Supplement of Atmos. Chem. Phys., 18, 5655–5675, 2018
https://doi.org/10.5194/acp-18-5655-2018-supplement

Atmospheric Chemistry and Physics
Open Access

Supplement of

Dynamics and composition of the Asian summer monsoon anticyclone

Klaus-Dirk Gottschaldt et al.

Correspondence to: Klaus-Dirk Gottschaldt (klaus-dirk.gottschaldt@dlr.de)

Contents

S1 Tracer-tracer diagrams

S1.1 Primer

Tracer-tracer diagrams show mixing ratios of two species encountered simultaneously and are a standard method for analyzing mixing processes in the UTLS region (e.g. Zahn et al., 2000; Vogel et al., 2011). Sampling of two different air masses that are in the process of mixing is indicated by a mixing line in the tracer-tracer diagram. The slope of the mixing line provides additional clues about the origin of the original air parcels ("end-members"). If the ratios of the end members remain constant over time, the slope of the mixing line is conserved, as long as the mixing process continues. If the mixing processes stops, the mixing lines converge to a single point in the tracer-tracer diagram. If the reservoir of one end-member is bigger than the other, points in the tracer-tracer diagram will be close to the dominating end-member. However, the relative size of the reservoirs does not affect the slope of mixing lines, thus allowing detection of even small entrainments. Slopes change in case of mixing ratio changes over time (e.g. via in situ production or loss) of one or both reservoirs. Different effects may lead to similar tracer-tracer relations, resulting in ambiguity when trying to reconstruct end-members or disentangling mixing and chemical effects. Furthermore, mixing lines in general exist in a multi-dimensional tracer space, and thus lines in a tracer-tracer plot need to be considered as projections onto 2d space. They might also be the result of mixing between more than two reservoirs. Additional dimensions (tracers) need to be considered to reduce ambiguities.

S1.2 Potential temperatures of the observations

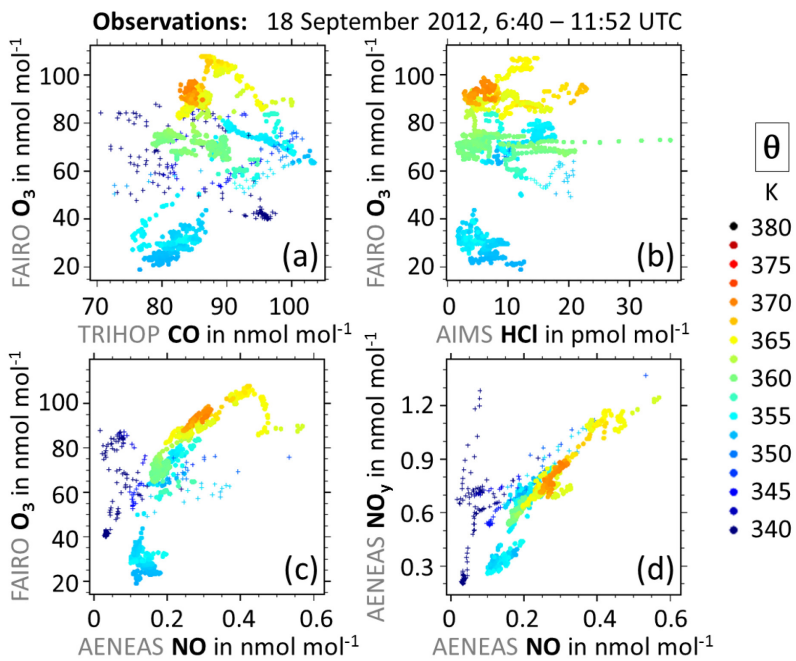

Figure S1. Measured data from the HALO ESMVal flight from Male to Larnaca. In contrast to Figs. 8cf, 9cf the samples here are color coded by their potential temperatures. During the dive (HALO descended from the upper to the lower troposphere and back to obtain profiles; indicated by crosses) potential temperatures were lower than shown, but the color scale is cut off at 340 K.

S2 Observations and model evaluation

S2.1 Simulated versus observed lightning activity

Convection is not explicitly resolved in the simulation, and the parameterizations for convection and lightning both introduce uncertainties to the simulation results for lightning. Uncertainties in the observations are due to a space- and time-dependent detection limit of 69% to 88%, and the application of a 3 month smoothing. Considering those uncertainties, the match between simulated and observed global distribution and frequency of lightning activity is reasonable (Fig. S2). In particular we note that also the observations over South Asia show stronger lightning activity during spring than during the monsoon season. The observed maximum of lightning activity over the coastal areas of Western Bengal and Bangladesh in April also shows up in the simulation.

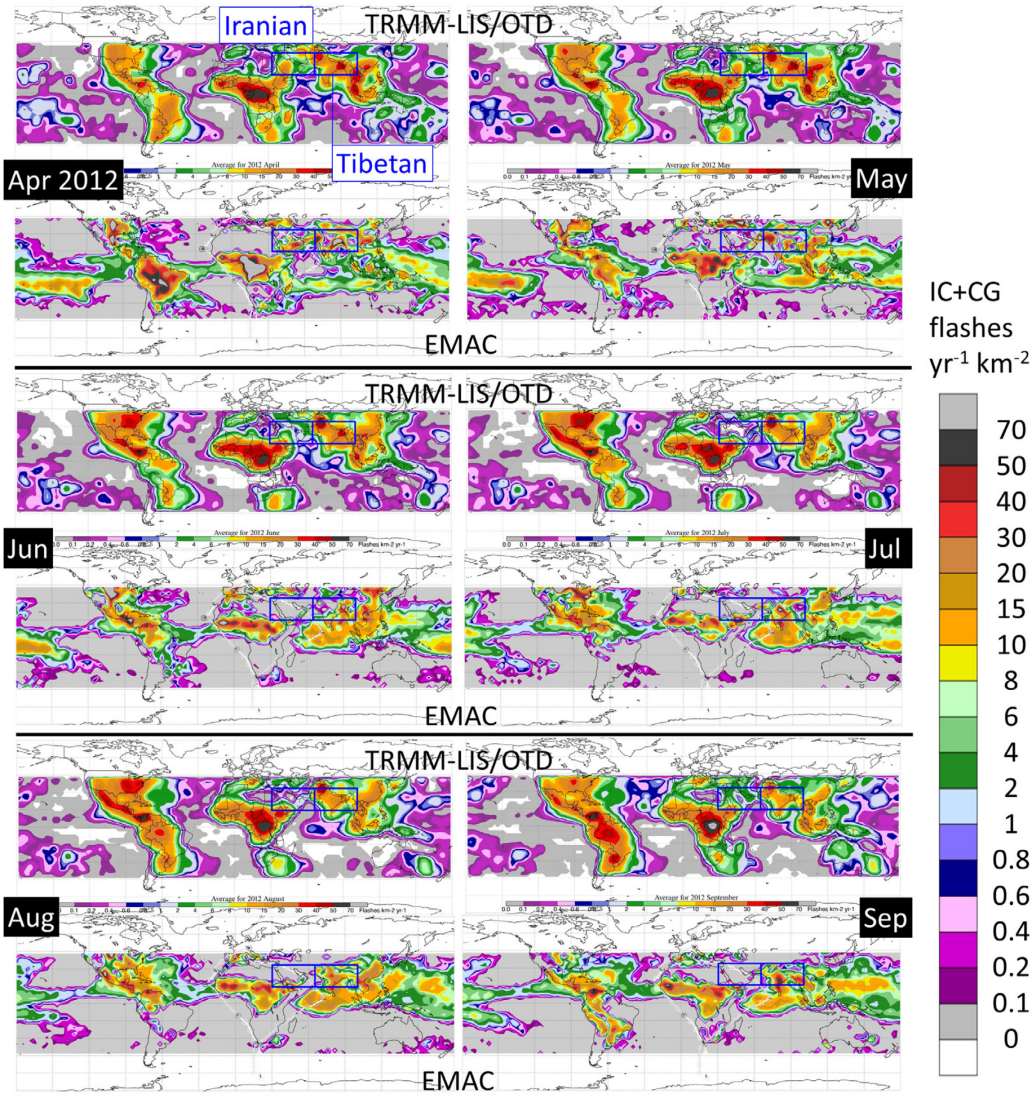

Figure S2. EMAC-simulated monthly mean lightning activity (intra-cloud + cloud-to-ground flash frequency) compared to the corresponding TRMM-LIS/OTD observations (Cecil, 2006). Data coverage and color scale are determined by the observations. Simulated lightning appears to be more localized, and thus exceeds the scale more often.

S2.2 Comparison of simulated NO and NO_y to IAGOS-CARIBIC observations

As noted in section 2, we compare simulated NO and NO_y to the corresponding IAGOS-CARIBIC observations (Fig. S3). Commercial airliners do not fly as high as HALO and the tracks hardly reach the southern ASMA fringe, but the northern ASMA edge and the center of the monsoon region have been sampled multiple times. We evaluated all 345 IAGOS-CARIBIC flights between 19 May 2005 and 9 April 2014, considering the respective latest data versions as of 10 November 2017. In total 86 flights between Frankfurt (IATA code: FRA) and Chennai (MAA) or Guangzhou (CAN) or Bangkok (BKK) transected the ASMA region. 32 of these flights provide NO data there, and 66 flights provide NO_y. Neglecting data below 300 hPa and subsampling to the time resolution of the simulation yields the numbers of comparable data that are given in Figs. S3bd. Given the above uncertainties related to the representation of $LiNO_x$ in the simulation, NO matches the corresponding IAGOS-CARIBIC observations surprisingly well (Fig. S3b). This holds also for the more robust (more data) global comparison (Fig. S3a). Increased $LiNO_x$ emissions in the ASMA region in spring are also consistent to IAGOS-CARIBIC, and the simulation might even slightly underestimate those emissions (Fig. S3b: MAM).

The simulation matches IAGOS-CARIBIC NO_y almost perfectly on the global scale (Fig. S3c), and only moderately overestimates it during summer in the ASMA region (Fig. S3d: JJA).

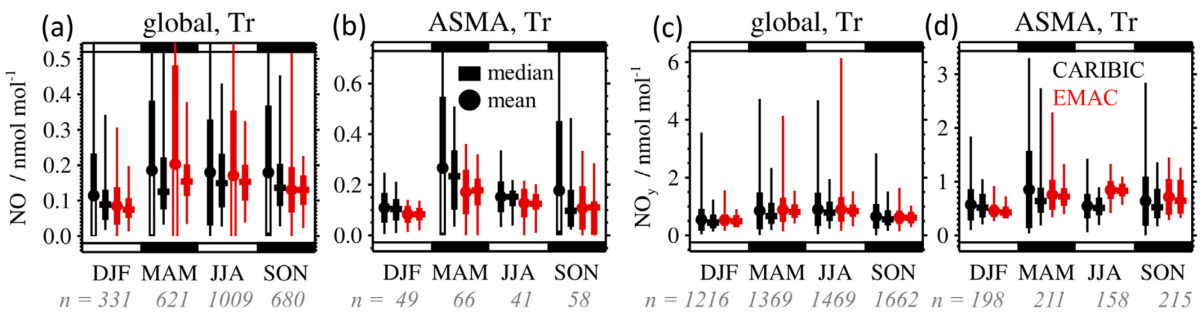

Figure S3. Comparison of IAGOS-CARIBIC (black) measurements in the altitude range between 300 hPa and the TP ("Tr") with corresponding results of the EMAC RC1SD-base-10a simulation (red) for (a) NO globally, (b) NO in the ASMA region (15-35°N, 30-100°E), (c) NO_y globally, (d) NO_y in the ASMA region. All data stem from the period May 2005 to April 2014. The simulation was sampled along the IAGOS-CARIBIC flight tracks with a resolution of 12 min, and IAGOS-CARIBIC observations were subsequently interpolated (interval mean) to a resolution of 12 min. Numbers n below the plots show the number of the remaining data pairs (after interpolation and filtering) available for the respective seasons. Dots represent mean values; whiskers indicate standard deviation, min & max values. Rectangles represent the median, and whiskers the percentiles 5, 25, 75, 95.

S3 Inter-annual variability

S3.1 Evolution of trace gas profiles in the Tibetan region 2010-2014

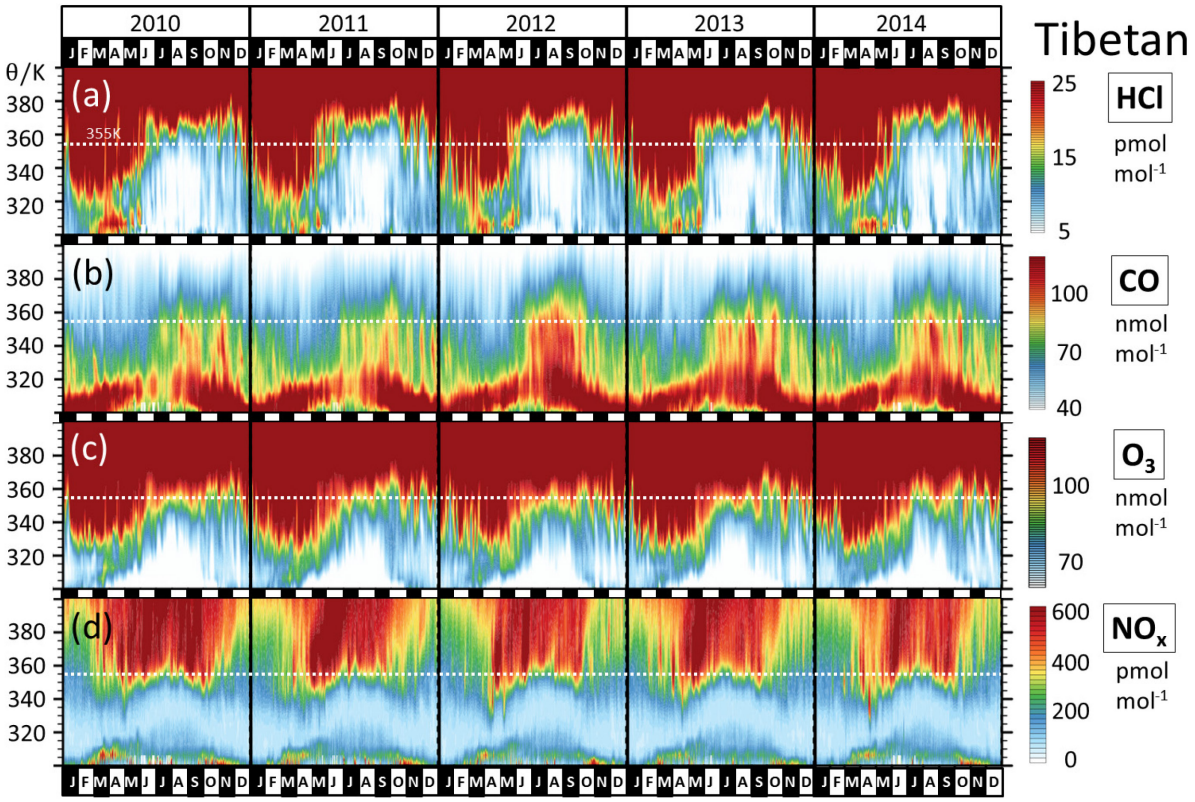

Figure S4. Evolution of simulated trace gas profiles and related diagnostics for the years 2010 - 2014 in the Tibetan ASMA region (15°N to 35°N , 65° - 100°E). Vertical coordinates are given as distance to the tropopause ("TP"), whose altitude depends on time and location. All values are grid-cell dry air mass weighted averages. The column for 2012 corresponds to Figs. 5, 6, 7, showing that the trace gas evolution in 2012 was largely similar to other years.

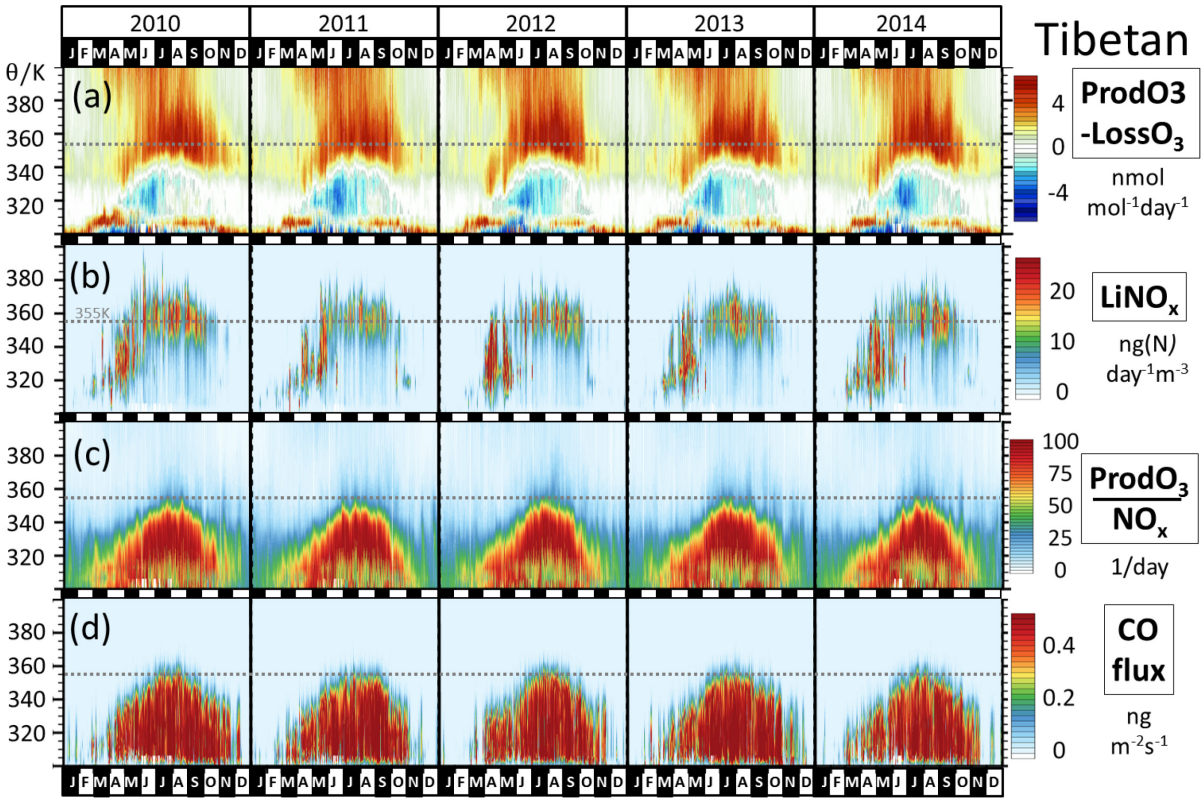

Figure S5. As Fig. S4, but putting Fig. 7 in a multi-annual perspective. Regarding the shown parameters, 2012 was a normal year.

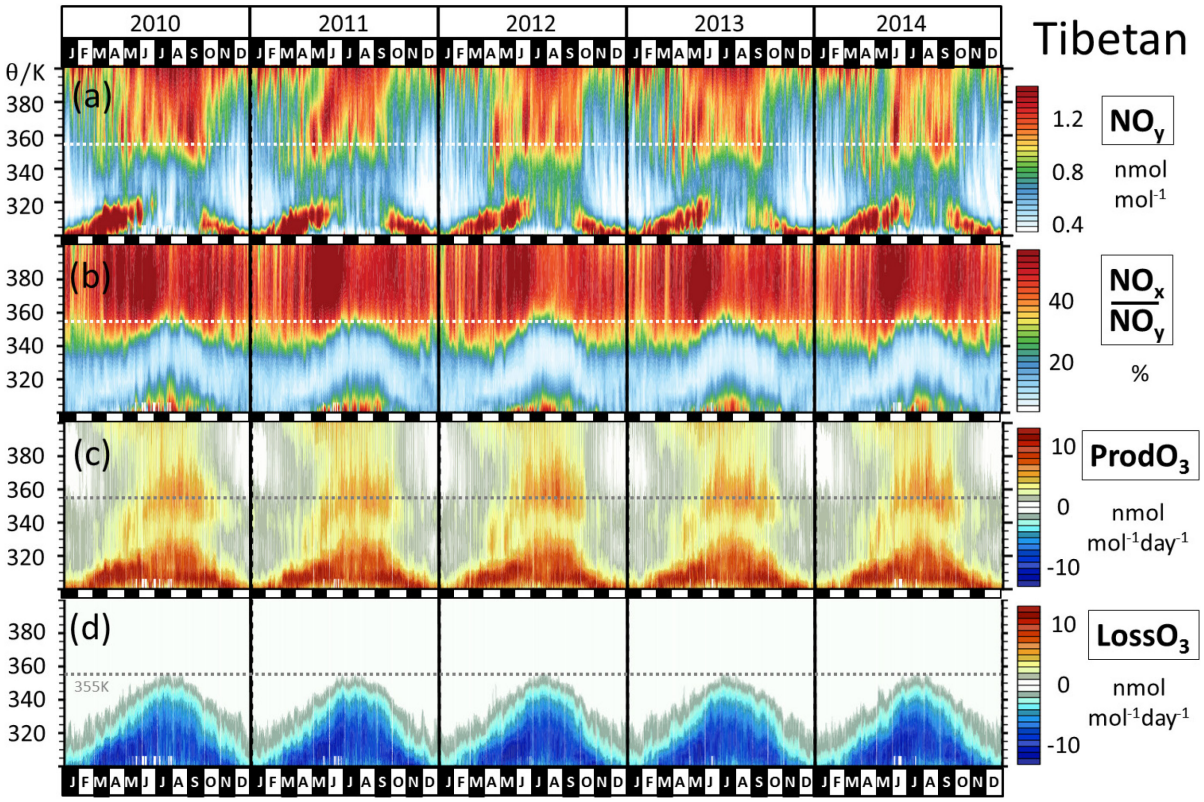

Figure S6. As Fig. S4, but putting Fig. 6 in a multi-annual perspective (Panels a and b). There is no noteworthy anomaly for 2012. Panels (c) and (d) show simulated photochemical O_3 production and destruction separately. $LossO_3$ is negligible at and above 355 K, thus the photochemical regime (NO_x-limited or NO_x–saturated) is determined mainly by $ProdO_3$.

S3.2 Evolution of trace gas profiles in the Iranian region 2010-2014

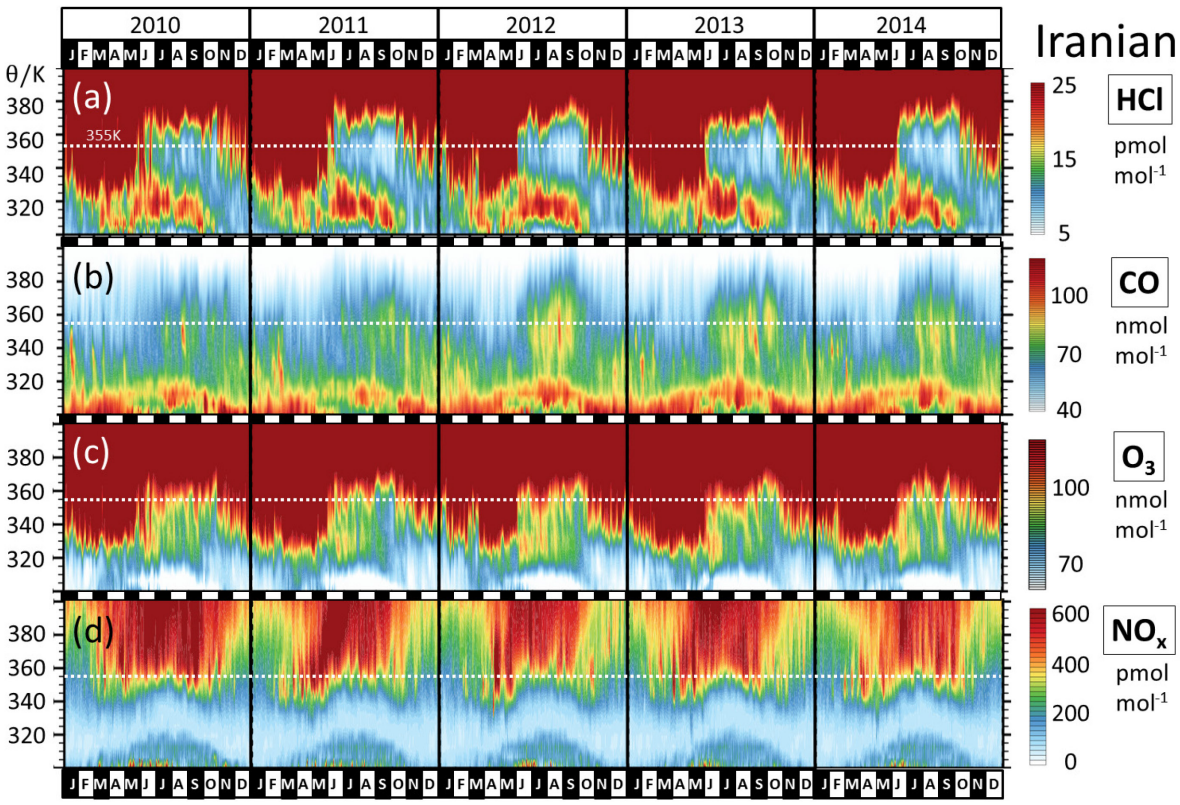

Figure S7. As Fig. S4, but for the Iranian ASMA region. Of the parameters shown, CO is the most variable one in the UTLS.

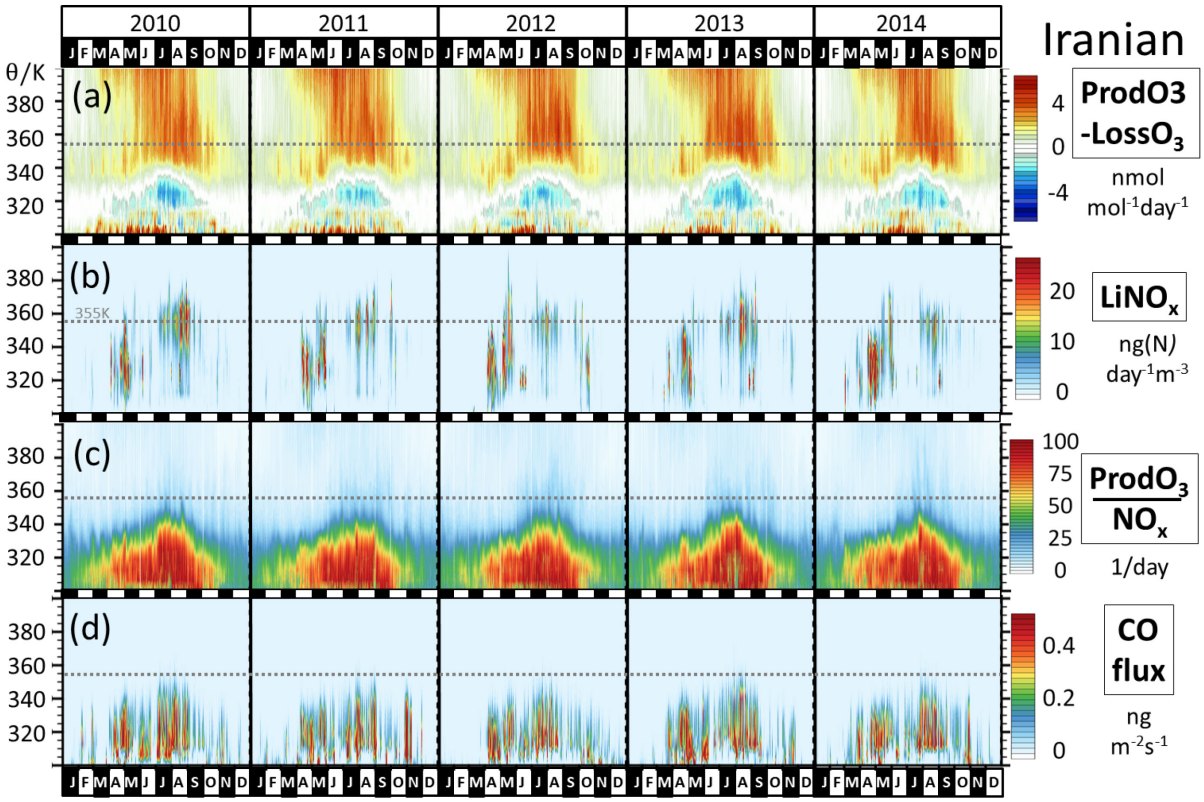

Figure S8. As Fig. S5, but for the Iranian region.

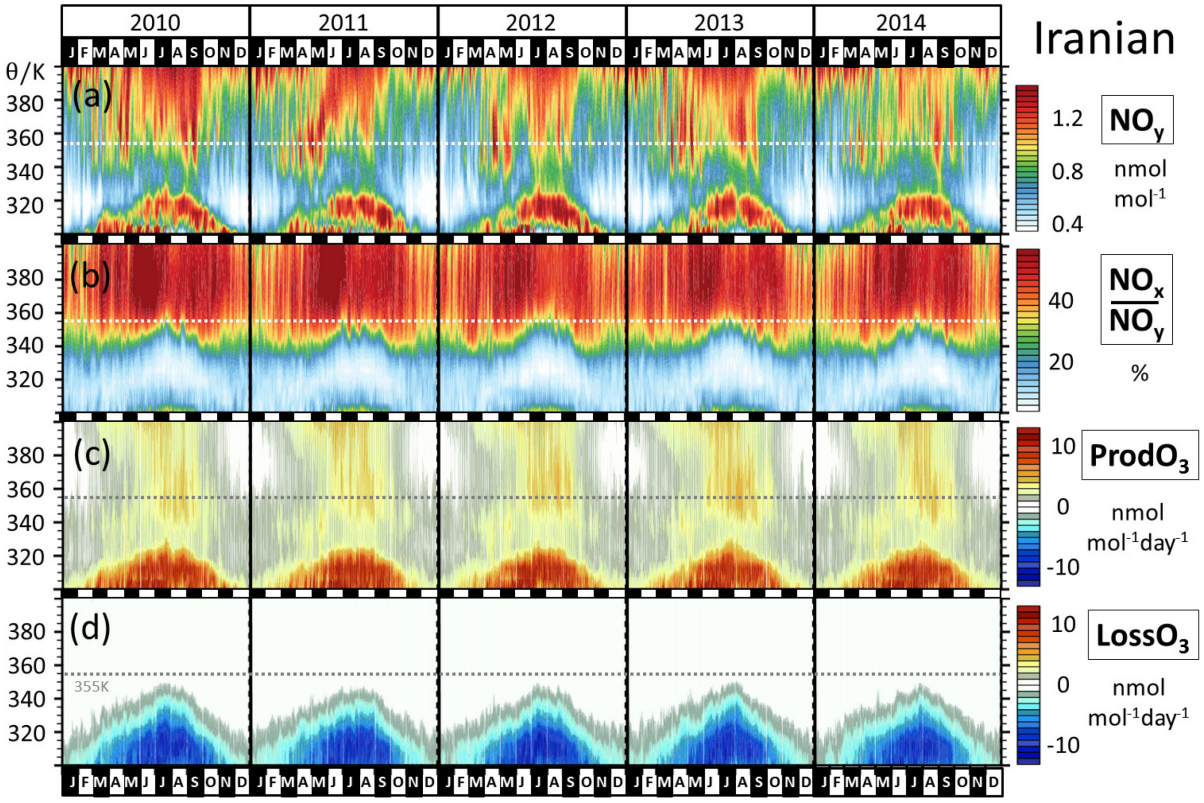

Figure S9. As Fig. S6, but for the Iranian region.

S3.3 TL entrainment 2010-2014

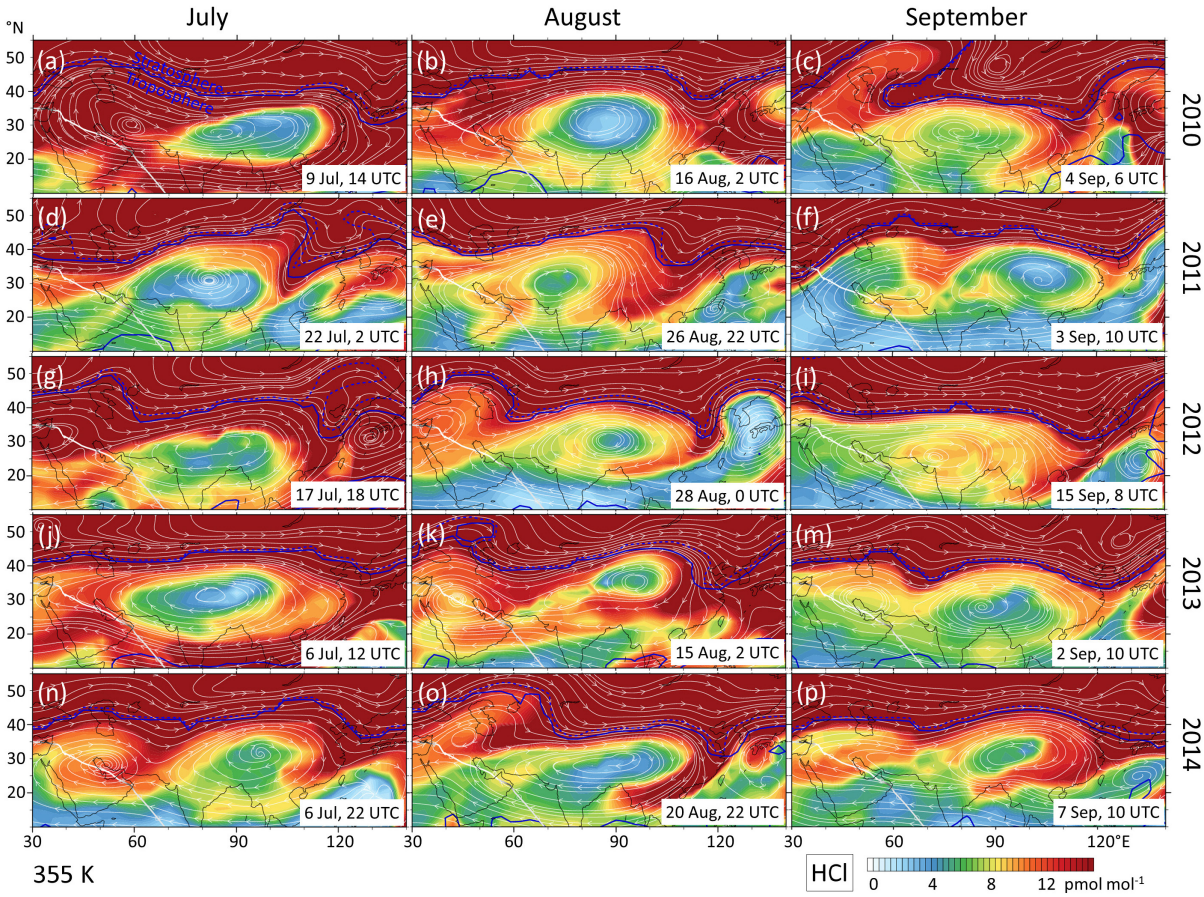

Figure S10. EMAC simulated HCl mixing ratios at 168 hPa in the ASMA region, complementing Fig. 3. The snapshots were selected to represent independent situations, where the southern ASMA fringe is marked by a filament of enhanced HCl. The filaments are often associated with a TP trough at the eastern ASMA flank. Enhanced HCl serves as a proxy for TL or stratospheric air.

S4 Trace gas profiles

S4.1. Simulated NO_y profiles

NO_y-profiles with maxima in the lower troposphere, in the UT and in the lower stratosphere dominate the Tibetan part (Fig. S11b). E-shaped NO_y-profiles in northern mid-latitudes (Grewe et al., 2001) were in part attributed to aviation NO_x emissions (Rogers et al., 2002), but aviation effects are much smaller in the tropics (Gottschaldt et al., 2013). Instead of aviation emissions, in situ production of lightning NO_x in the prevalent thunderstorms of the monsoon season increases NO_y in the UT over South Asia (Figs. 6d, 7d).

Photochemical production of HNO_3 and thus NO_y mixing ratios also increase with altitude above the tropopause (Seinfeld and Pandis, 2006). However, NO_y mixing ratios in the region between the tropopause and 15 hPa above the tropopause are often smaller than in the adjacent altitudes. There is little in situ production and not much transport from above or below. The maximum in the lower troposphere can be attributed to boundary layer pollution, but at about 400 hPa below the tropopause mostly non-solvable components (e.g. NO_x) are left.

Profiles in the Iranian ASMA part (Fig. 6c) have a different history of origins, and with just one minimum in the mid-troposphere are mostly C-shaped (Fig. S11a). During summer the Arabian Peninsula is dry. Deep convection (as indicated by lightning NO_x emissions in Fig. 7c) is mainly localized in the south-western Yemen region (Fig. 10), i.e. at the edge of the region we defined for calculating profiles of the Iranian part of the ASMA. Washing out is negligible throughout most of the Iranian region, and therefore NO_y can rise to about 400 hPa below the tropopause (circled in Fig. 6c).

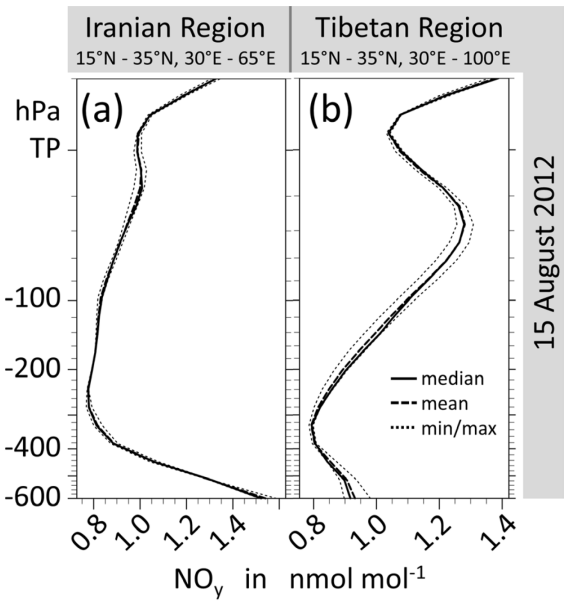

Figure S11. Simulated profiles of NO_y as simulated for 15 August 2012. These are examples of a C-shaped profile in the Iranian region (a) and an E-shaped profile in the Tibetan region (b).

S5 Processes

S5.1 Lightning NO_x sensitivity simulations

In order to link the $LiNO_x$ emissions to the NO_x burden in the ASMA region, a suite of EMAC sensitivity simulations with modified emission factors was conducted (Figs. S12, S13). All EMAC analyses in the main text are based on simulation RC1SD-base-10a (Jöckel et al., 2016), which is given in Fig. S12 just for comparison. The other simulations discussed in the context of Figs. S12 and S13 here are derived from EMAC simulation RC1SD-base-10, which differs in road traffic emissions and optical properties of stratospheric aerosol (Jöckel et al., 2016) from RC1SD-base-10a. Total $LiNO_x$ emissions in RC1SD-base-10 are 4.6 Tg(N) in 2012 (Jöckel et al., 2016), which is in the realistic range of 2 – 8 Tg(N) yr^{-1} (Schumann and Huntrieser, 2007). RC1SD-base-10 and our base simulation for the $LiNO_x$ sensitivity analysis (b01) are both operated in chemistry-climate model (CCM) mode, i.e. including interactive chemistry with feedback on dynamics. Simulation b01 differs only in the usage of daily (Kaiser et al., 2012) instead of monthly biomass burning emissions and 5 h instead of 10 h output intervals. Feedbacks from chemistry on dynamics in all quasi chemistry-transport model mode (QCTM) (Deckert et al., 2011) simulations are based on identical trace gas time series from b01. The same dynamics incl. convection is simulated in all QCTM simulations. Differences between a QCTM reference simulation (q01) and sensitivity simulations (s*) are thus exclusively due to chemical perturbations. All QCTM simulations cover June – September 2012, but the first 3 months were discarded for spin-up.

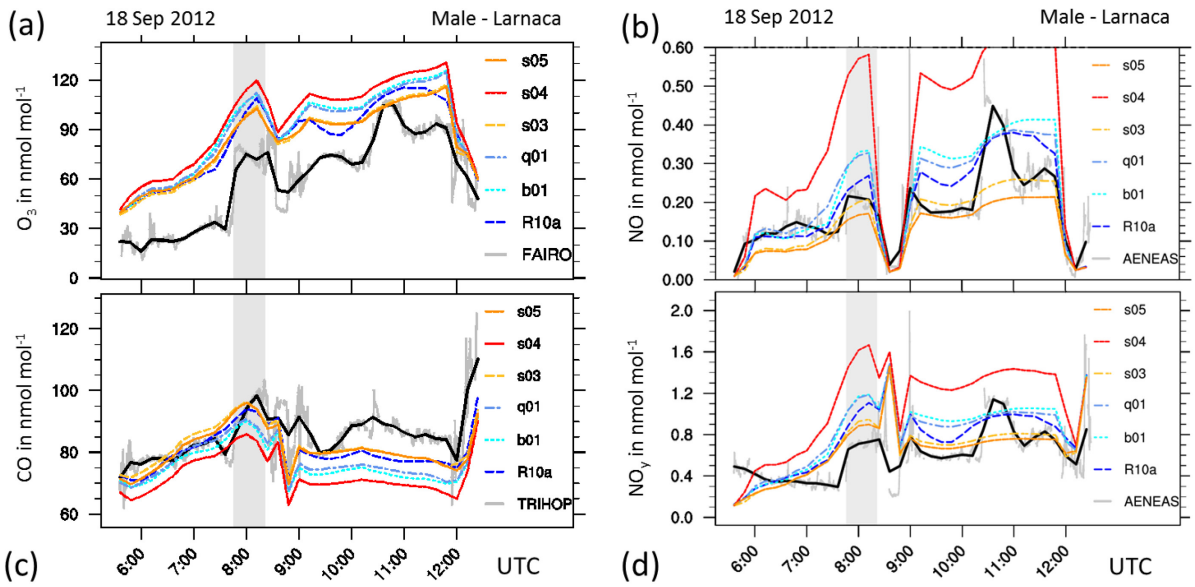

Figure S12. Mixing ratios of O_3, CO, NO and NO_y along the HALO flight track from Male to Larnaca, on 18 September 2012. Grey shading marks the first flight section in ASMA air. Grey line: in situ measurements in 10 s resolution, black: in situ averaged to 12 min simulation time steps, R10a: EMAC simulation RC1SD-base-10a. Sensitivity simulations are based on the almost identical RC1SD-base-10 simulation of (Jöckel et al., 2016), feature daily instead of monthly biomass burning emissions, and were performed in quasi chemistry transport model mode (Deckert et al., 2011) to facilitate isolating the effects of modified emissions.

b01: as R10a, but with different traffic and different biomass burning emissions; q01: as b01, but QCTM; s03: as q01, but halved $LiNO_x$ emissions; s04: as q01, but doubled $LiNO_x$ emissions; s05: as s03, but with a different vertical emission profile of $LiNO_x$ (emission factors not decreased in the mid-troposphere, i.e. no C-shape)

Figure S12 shows that RC1SD-base-10a captures observed O_3, CO, NO and NO_y along the HALO ESMVal flight path slightly better than b01 and q01. We are yet confident that the overall agreement is good enough for the analysis of chemical perturbations. For the QCTM sensitivity analyses it is more important to note that differences between b01 and q01 are negligible.

Figure S13k shows that halving $LiNO_x$ emission factors results in almost halved NO_x in the uppermost troposphere. Doubling of $LiNO_x$ emissions leads to almost doubled NO_x just below the tropopause (Fig. S13m). The biggest relative sensitivity in Fig. S13km almost coincides with the altitude range of the largest NO_x mixing ratios just below the tropopause (Fig. S13j). Thus, in our simulations $LiNO_x$ clearly dominates the NO_x budget from the tropopause to 100 hPa below it. The impact of LiNOx fades out at lower altitude, and almost vanishes at 400 hPa below the tropopause. This is consistent with the profiles of $LiNO_x$ emissions in September 2012, which mainly occur in the Tibetan part of the ASMA (Fig. 7d).

Modifications of NO_x print through on other O_3 precursors mainly via changes to the atmospheric oxidizing capacity (OH: Figs. S13ghi). In response to halved $LiNO_x$, OH decreases 200 hPa below the tropopause and lower, and increases above (Fig. S13h). The effects are reversed for doubled $LiNO_x$ (Fig. S13i). The largest relative effects coincide with largest absolute OH mixing ratios.

CO decreases throughout the shown altitude range for halved $LiNO_x$ (Fig. S13e). Without major production terms in the UT, modifications to CO mixing ratios are dominated by the loss reaction $CO + OH \rightarrow H + CO_2$. The rate coefficient of this reaction is proportional to pressure, and otherwise depends only on constants (supplement to Jöckel et al. (2016)). Laterally averaged CO mixing ratios vary little from 50 to 400 hPa below the tropopause (Fig. S13d), but are affected by decreased and increased OH (Figs. S13fg). Decreased OH in the lower half of the domain dominates the overall CO response. CO rises through this region with higher pressures before reaching the UT in the Tibetan part of the ASMA (Fig. 5d), which obviously outweighs the CO response to increased OH in the UT of Tibetan and Iranian part combined. Increased OH 200 – 500 hPa below the tropopause consequently leads to an overall decrease of CO in response to doubled $LiNO_x$ (Fig. S13f). The O_3 precursors NO_x and CO display opposite trends in response to $\Delta LiNO_x$.

Curiously, HCl shows the opposite response to modified $LiNO_x$ (Figs. S13abc). There is no chemical production of HCl in the UT, and the only loss term in the simulations is $HCl + OH \rightarrow Cl + H_2O$. The rate coefficient of this reaction is 1.7E-12 * EXP(-230/Temperature), see supplement to Jöckel et al. (2016). However, the tropospheric response of HCl to ΔOH is dominated rather by the vertical profile of HCl mixing ratios than by lower temperatures towards the tropopause. Almost all HCl in the UT is of stratospheric origin, and HCl mixing ratios steeply increase across the tropopause. Thus the UT response of HCl is dominated by ΔOH near the tropopause: increased OH for halved $LiNO_x$ increases HCl losses, and vice versa for doubled $LiNO_x$.

The response of UT net O_3 production to $\Delta LiNO_x$ (Figs. S13qrs) has mostly the same sign as ΔNO_x. As noted already in the context of Fig. 5 and Fig. 6, opposite gradients of O_3 precursors NO_x and CO in the UT lead to a broad altitude range of enhanced net O_3 production in the ASMA centered about 100 hPa below the tropopause. O_3 production is limited by NO_x in lower altitudes and by CO (and other volatile organic compounds) towards the tropopause. NO_x and CO display opposite trends in response to $\Delta LiNO_x$, but relative changes to NO_x are larger and dominate the overall response of net O_3 production. We note, however, that the largest increase of

NO_x at the end of September (circled in Fig. S13m) decreases net O_3 production to zero or even net loss (circled in Fig. S13s), indicative of the NO_x-limited photochemical regime.

O_3 mixing ratios respond to $\Delta LiNO_x$ essentially like net O_3 production in the UT (Figs. S13nop). The altitude of maximum relative ΔO_3 is slightly lower than the altitude of maximum absolute changes to net O_3 production. We attribute this effect to upwards increasing absolute O_3 mixing ratios.

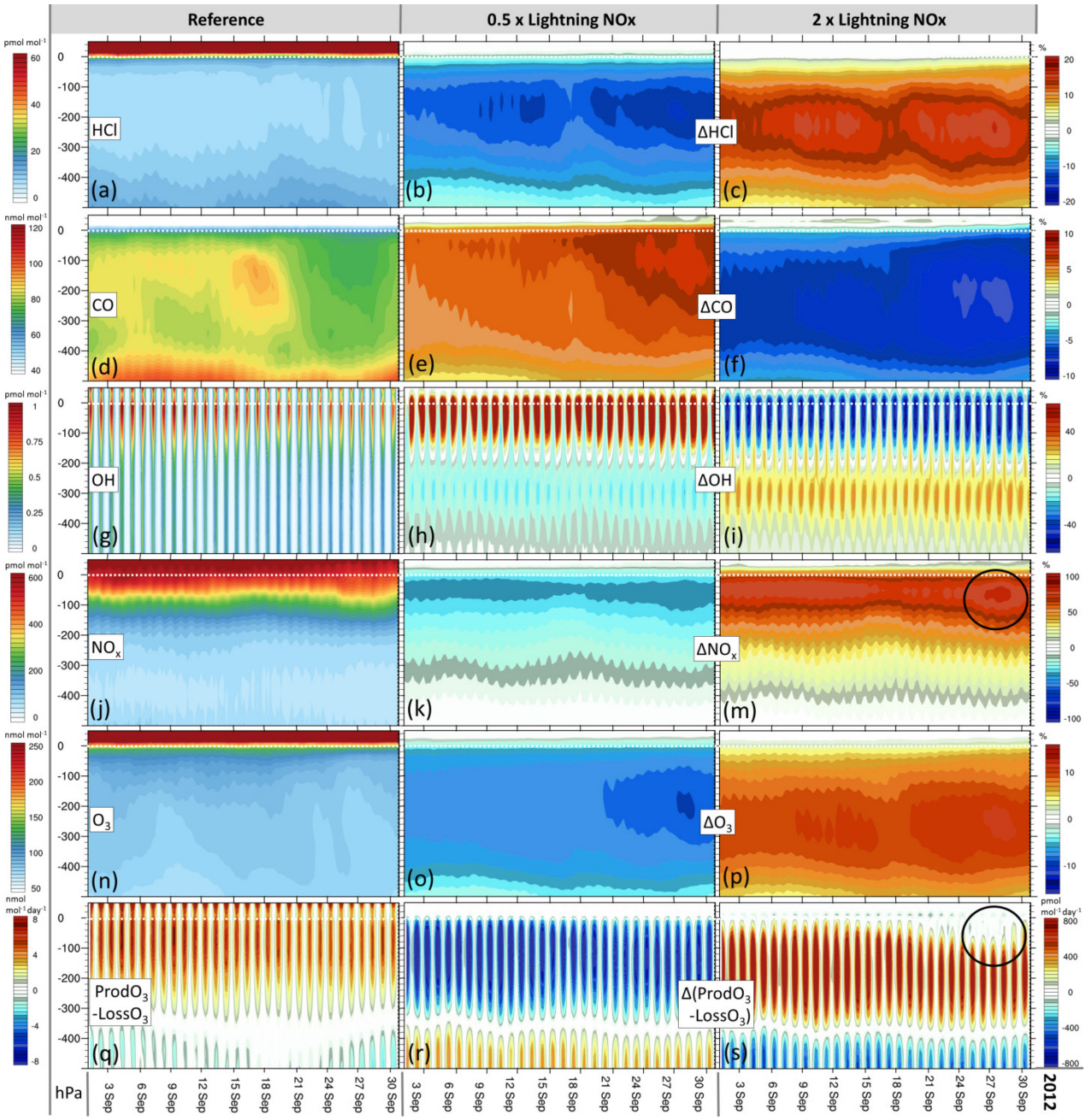

Figure S13. Evolution of simulated trace gas profiles and related diagnostics during September 2012 in the ASMA region (15° N – 35° N, 30° E – 100° E), and their sensitivity to $LiNO_x$ emissions. The vertical axes cover the UTLS and middle troposphere, and their coordinates are given as pressure distance to the tropopause. Left column: QCTM reference simulation (q01). Middle column: s03 – q01, relative deviation of sensitivity simulation s03 with respect to q01 for trace gases, absolute deviation for net O_3 production. Right column: s04 – q01.

S5.2 Entrainment of lower tropospheric air

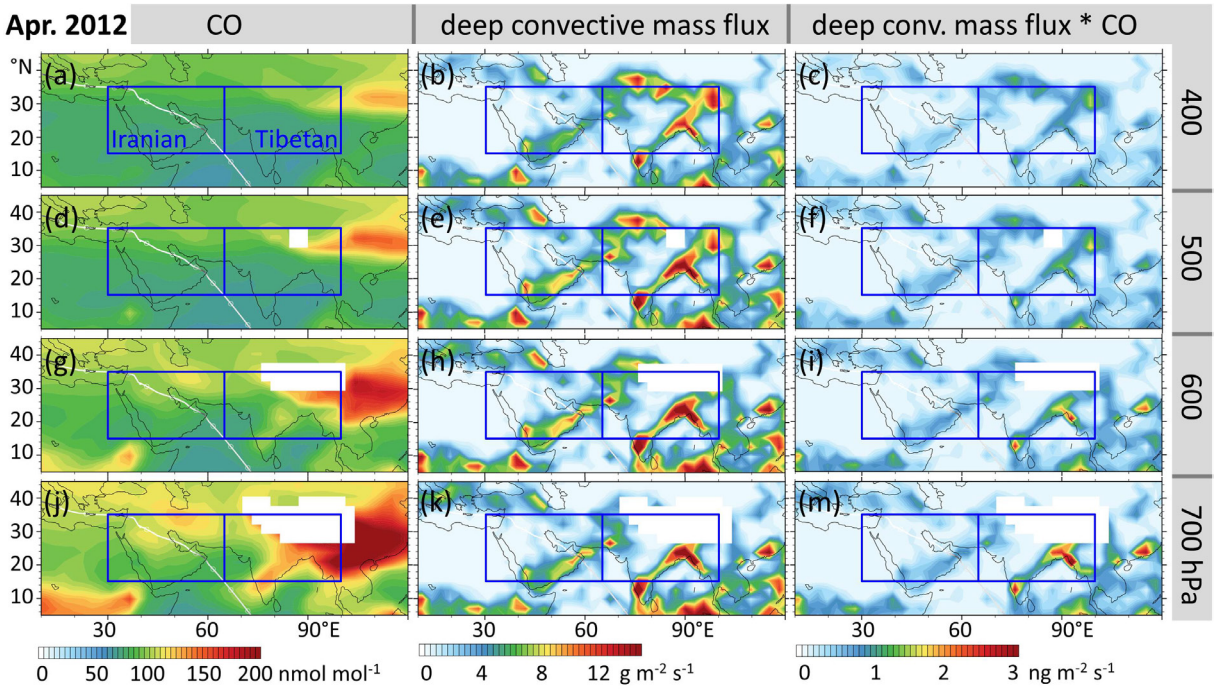

Figure S14. EMAC-simulated monthly mean distributions of CO (left) and deep convective mass flux (middle) in different pressure altitudes during spring (April 2012). The right column shows the deep convective mass flux of CO based on individual output steps. Blue rectangles mark the outline of the regions used to produce Figs. 5, 6, 7.

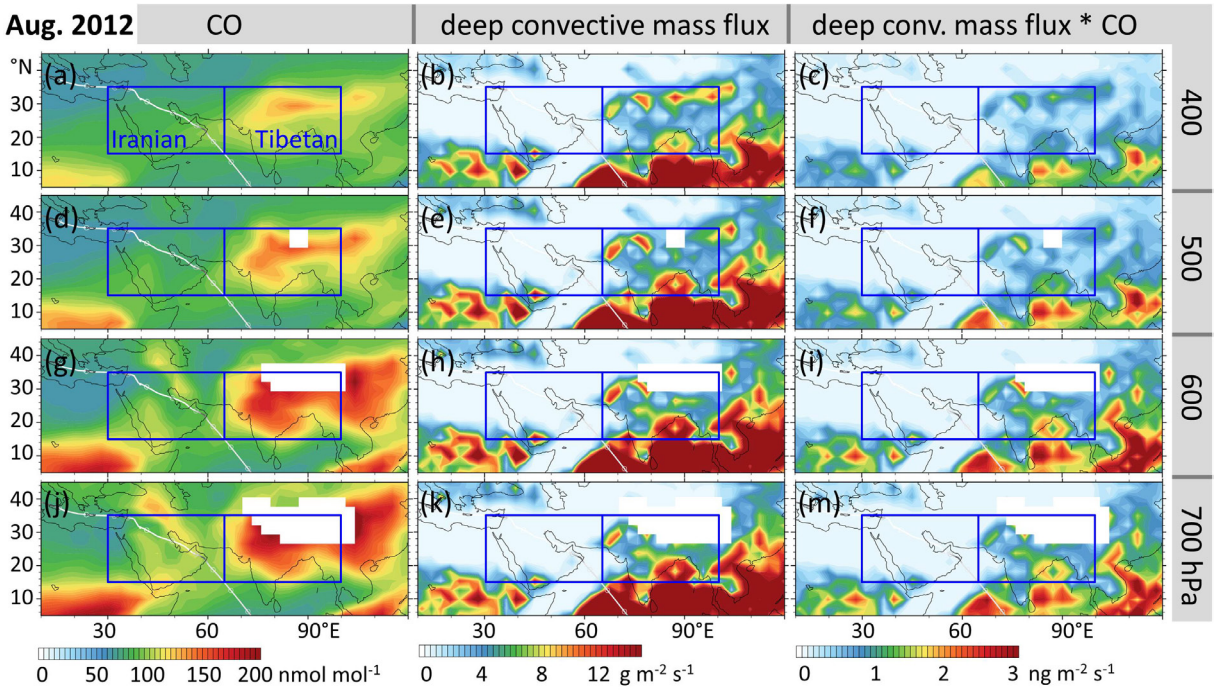

Figure S15. As Fig. S14, but for August 2012, i.e. during the monsoon season.

S5.3 Photochemical O_3 production

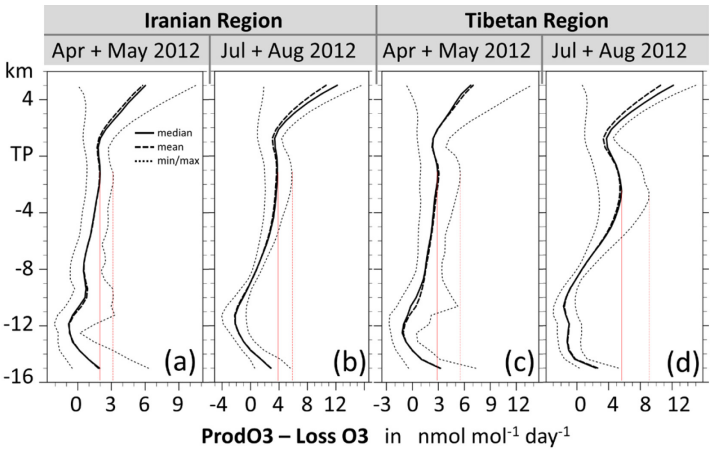

Figure S16. Simulated profiles of net O_3 production in the Tibetan region. Auxiliary red lines indicate the mean and maximum net O_3 production in the UT, which are both higher in summer than in spring.

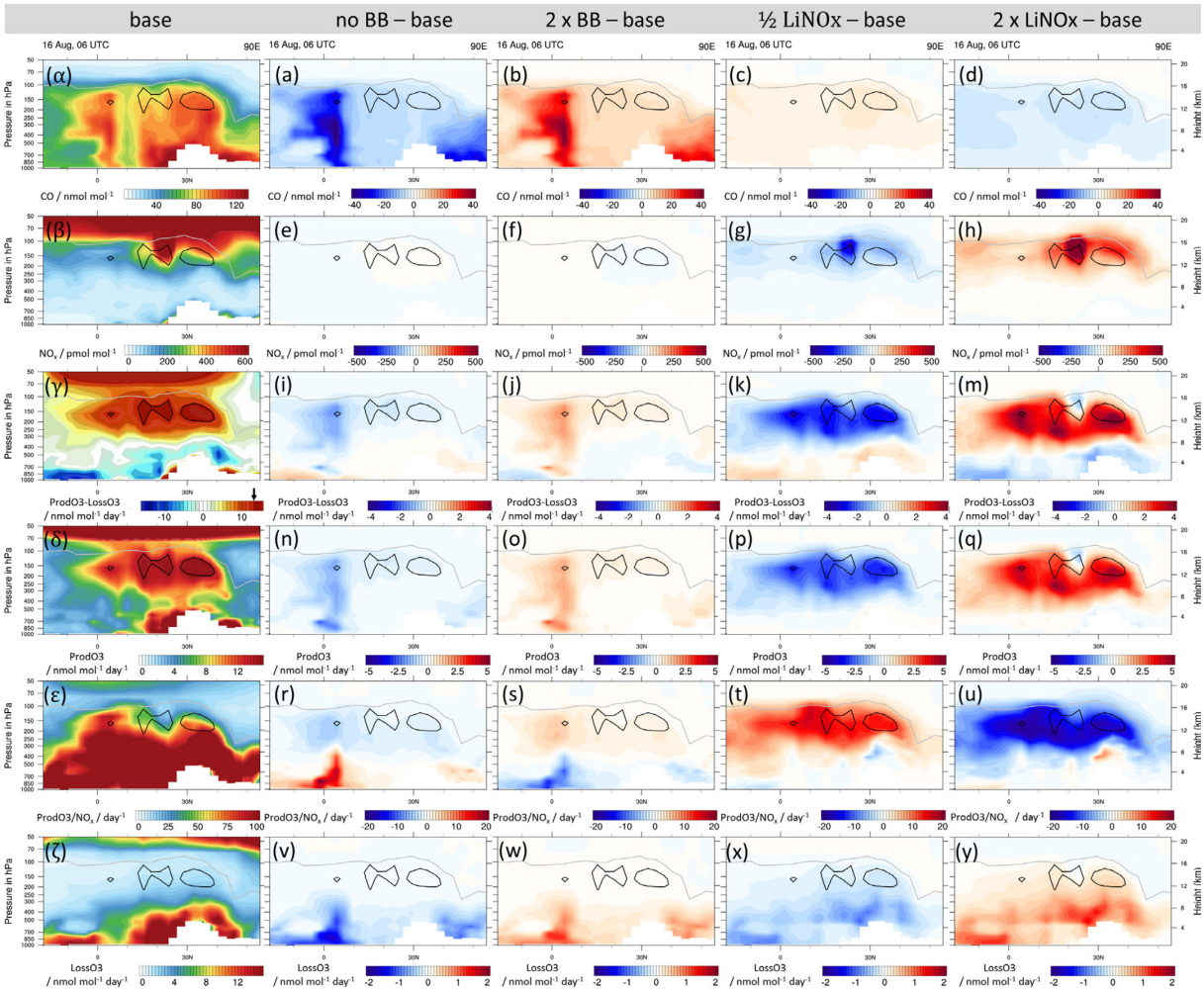

Figure S17. Selection of parameters related to photochemical O_3 production in a meridional curtain through the Tibetan part of the ASMA in a snapshot taken mid August 2012. The left column shows the results of the EMAC QCTM simulation that has been introduced in appendix A. The other columns show the difference of that reference to sensitivity simulations, which feature identical dynamics but differ in biomass burning (BB) and lightning NO_x (LiNOx) emissions. The black lines represent the 13 nmol mol^{-1} day^{-1} isocontour of net O_3 production (taken from panel γ); the grey line denotes the tropopause.

S5.4 Splitting-up and stirring

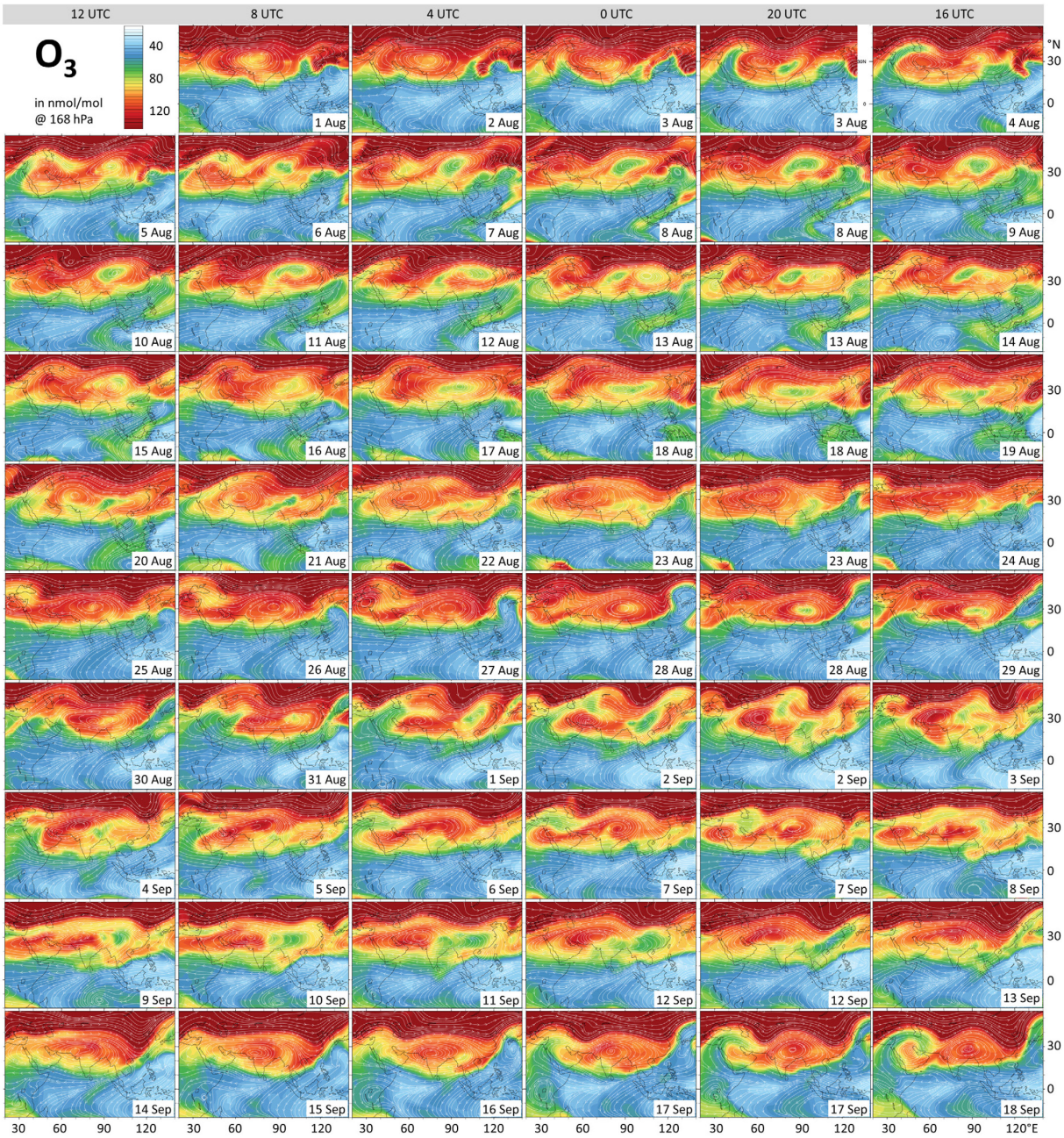

Figure S18. EMAC simulated O_3 mixing ratios and streamlines at 168 hPa in the ASMA region. The snapshots are 20 hours apart and cover the period from 1 August to 18 September 2012.

Larger fractions of the O_3-rich fringe were entrained during splitting up events. The sequence of snapshots (Fig. S18) covers almost half a monsoon season and episodic O_3-poor upwellings over the Tibetan plateau are smaller and shorter lived than O_3-rich regions at 168 hPa. This is consistent to the long-term average at a corresponding isentropic level (Fig. 1i).

References

Cecil, D. J.: LIS/OTD 2.5 Degree Low Resolution Monthly Climatology Time Series (LRMTS): Data set available online from the NASA Global Hydrology Resource Center DAAC, Huntsville, Alabama, U.S.A. doi: http://dx.doi.org/10.5067/LIS/LIS-OTD/DATA311, access: https://lightning.nsstc.nasa.gov/data/data_lis-otd-climatology.htm, 18. September 2017, 2006.

Deckert, R., Jöckel, P., Grewe, V., Gottschaldt, K., and Hoor, P.: A quasi chemistry-transport model mode for EMAC, Geoscientific Model Development, 4, 195-206, 10.5194/gmd-4-195-2011, 2011.

Gottschaldt, K., Voigt, C., Jöckel, P., Righi, M., Deckert, R., and Dietmüller, S.: Global sensitivity of aviation NOx effects to the HNO3-forming channel of the HO2 + NO reaction, Atmospheric Chemistry and Physics, 13, 3003-3025, 10.5194/acp-13-3003-2013, 2013.

Grewe, V., Brunner, D., Dameris, M., Grenfell, J. L., Hein, R., Shindell, D., and Staehelin, J.: Origin and variability of upper tropospheric nitrogen oxides and ozone at northern mid-latitudes, Atmospheric Environment, 35, 3421-3433, 2001.

Jöckel, P., Tost, H., Pozzer, A., Kunze, M., Kirner, O., Brenninkmeijer, C. A. M., Brinkop, S., Cai, D. S., Dyroff, C., Eckstein, J., Frank, F., Garny, H., Gottschaldt, K.-D., Graf, P., Grewe, V., Kerkweg, A., Kern, B., Matthes, S., Mertens, M., Meul, S., Neumaier, M., Nützel, M., Oberländer-Hayn, S., Ruhnke, R., Runde, T., Sander, R., Scharffe, D., and Zahn, A.: Earth System Chemistry integrated Modelling (ESCiMo) with the Modular Earth Submodel System (MESSy) version 2.51, Geoscientific Model Development, 9, 1153-1200, 10.5194/gmd-9-1153-2016, 2016.

Kaiser, J. W., Heil, A., Andreae, M. O., Benedetti, A., Chubarova, N., Jones, L., Morcrette, J. J., Razinger, M., Schultz, M. G., Suttie, M., and van der Werf, G. R.: Biomass burning emissions estimated with a global fire assimilation system based on observed fire radiative power, Biogeosciences, 9, 527-554, 10.5194/bg-9-527-2012, 2012.

Rogers, H., Teyssedre, H., Pitari, G., Grewe, V., van Velthoven, P., and Sundet, J.: Model intercomparison of the transport of aircraft-like emissions from sub- and supersonic aircraft, Meteorologische Zeitschrift, 11, 151-159, 10.1127/0941-2948/2002/0011-0151, 2002.

Schumann, U., and Huntrieser, H.: The global lightning-induced nitrogen oxides source, Atmos. Chem. Phys., 7, 3823-3907, 2007.

Seinfeld, J. H., and Pandis, S. N.: Atmospheric chemistry and physics : from air pollution to climate change, 2nd edition ed., John Wiley & Sons, Inc., Hoboken, New Jersey, 2006.

Vogel, B., Pan, L. L., Konopka, P., Günther, G., Müller, R., Hall, W., Campos, T., Pollack, I., Weinheimer, A., Wei, J., Atlas, E. L., and Bowman, K. P.: Transport pathways and signatures of mixing in the extratropical tropopause region derived from Lagrangian model simulations, Journal of Geophysical Research, 116, 10.1029/2010jd014876, 2011.

Zahn, A., Brenninkmeijer, C. A. M., Maiss, M., Scharffe, D. H., Crutzen, P. J., Hermann, M., Heintzenberg, J., Wiedensohler, A., Güsten, H., Heinrich, G., Fischer, H., Cuijpers, J. W. M., and van Velthoven, P. F. J.: Identification of extratropical two-way troposphere-stratosphere mixing based on CARIBIC measurements of O3, CO, and ultrafine particles, Journal of Geophysical Research: Atmospheres, 105, 1527-1535, 10.1029/1999jd900759, 2000.